European **J**ournal of **Chem**istry

APH
ATLANTA PUBLISHING HOUSE

Hydrothermally synthesized (*N,O*)-linked Cu(II)-based coordination complex as a potential antibacterial agent

Anmol Chettri [ID], Sudarshan Pradhan [ID], Pritika Gurung [ID], Sriparna Roy [ID] and Biswajit Sinha [ID] *

Department of Chemistry, University of North Bengal, Darjeeling, 734013, India

* Corresponding author at: Department of Chemistry, University of North Bengal, Darjeeling, 734013, India.
 e-mail: biswachem@nbu.ac.in (B. Sinha).

ABSTRACT

The *N,O*-linked Cu(II)-based coordination complex was synthesized hydrothermally and characterized by SC-XRD, FTIR spectroscopy, and FE-SEM. Single crystal X-ray diffraction studies showed that the complex crystallizes in a square pyramidal geometry and belongs to the monoclinic crystal system with the space group $P2_1/n$. Crystal data for $C_{14}H_{13}CuN_3O_6$: $a = 8.7355(11)$ Å, $b = 17.646(2)$ Å, $c = 9.8036(12)$ Å, $\beta = 98.506(6)°$, $V = 1494.6(3)$ Å^3, $Z = 4$, $\mu(MoK\alpha) = 1.500$ mm^{-1}, $Dcalc = 1.701$ g/cm^3, 5120 reflections measured ($4.616° \leq 2\Theta \leq 49.982°$), 1953 unique ($R_{int} = 0.0316$, $R_{sigma} = 0.0718$) which were used in all calculations. The final R_1 was 0.0380 (I > 2σ(I)) and wR_2 was 0.0972 (all data). The experimental antibacterial activity studies performed using the disc diffusion method revealed that the complex is indeed acting as a good antibacterial agent against *Staphylococcus aureus* and *Escherichia coli.* A better understanding of the binding mechanisms was uncovered through comparative molecular docking investigations. The docking score for the target *S. aureus glyrase* complex with DNA (PDB id-2XCS) was found to be -7.1 kcal/mol, while the docking score for dialkylglycine decarboxylase (PDB id-1D7U) was -5.2 kcal/mol. The high docking score of the complex with the target protein allowed the complex to act as a potential antibacterial agent. These results were also supported by other theoretical studies such as DFT calculations and pharmacokinetic studies. The correlation between the HOMO-LUMO energy gap and antibacterial activity was studied computationally. Hirshfeld surface analysis and pharmacokinetic studies were also performed for this crystal for a better understanding of the intermolecular interactions and ADME properties.

1. Introduction

Due to the astounding architectures, topologies and diverse potential applications as catalysts and chemical sensors, the design and synthesis of coordination complexes has attracted tremendous attention globally [1-4]. Many factors, including the geometry of coordination preferred by a specific metal ion, pH, nature of the counterions, temperature, and ligand geometry, can influence the architecture and functions of the products [5]. The hydrothermal synthesis of metal complexes has recently received considerable attention because it is one of the greener ways of synthesizing a complex. Unlike many other advanced synthetic methods, the hydrothermal method uses relatively inexpensive instrumentation and precursors [6]. From an environmental standpoint, this method is more environmentally benign than many other synthetic methods [7-11]. Furthermore, by this method, we can readily obtain or control the rate and uniformity of nucleation, crystal formation, and aging, all of which affect the crystal size, morphology, and aggregation. This simple method requires no catalyst, toxic and expensive surfactant, or template, making it an ideal method for large-scale manufacturing of high-quality, dislocation-free single crystals.

Because Cu(II) is biologically important, the synthesis of various biologically useful Cu(II) complexes is becoming an urgent need. Cu(II) ions and their complexes have continued to catch the eye of coordination chemists because of their diverse structural features, utility as models for the active centres of various metalloenzymes, catalytic, electronic, magnetic and biological properties [12-14].

Dipicolinic acid is a good candidate for coordination with transition metals in this respect because of its ability to form chelates through its two *O* atoms and one *N* atom, which provides extra stability to the complex formed. Pyridine-2,6-dicarboxylic acid (H₂dipic) is a polydentate ligand that can form stable chelates with oxo-metal cations and simple metal ions, thus exhibiting a wide variety of coordination behaviours. Dipicolinates (dipic) are often coordinated with transition metal ions through carboxylate bridges between the metal centres, forming dimeric or polymeric complexes [15-18] or by tridentate chelation (O, N, O') to a single metal ion [17,18]. Dipicolinic acid has its applications in analytical chemistry [19], corrosion inhibition, nuclear reactor decontamination [20], and many biological activities [21]. Benzimidazole (BMZ), a heterocyclic aromatic compound, is very well known for its antimicrobial properties [22].

In this study, we report the synthesis of a Cu (II)-based coordination complex having the molecular formula C₁₄H₁₁Cu N₃O₅·H₂O using Cu(NO₃)·2H₂O, pyridine-2,6-dicarboxylic acid and benzimidazole using the hydrothermal method. Although

Table 1. Crystal data and structure refinement for complex.

Empirical formula	$C_{14}H_{13}N_3O_6Cu$
Formula weight (g/mol)	382.81
Temperature (K)	296(2)
Crystal system	Monoclinic
Space group	$P2_1/n$
a, (Å)	8.7355(11)
b, (Å)	17.646(2)
c, (Å)	9.8036(12)
β (°)	98.506(6)
Volume (Å³)	1494.6(3)
Z	4
ρ_{calc} (g/cm³)	1.701
μ (mm⁻¹)	1.500
F(000)	780.0
Crystal size (mm³)	0.18 × 0.17 × 0.16
Radiation	MoKα (λ = 0.71073)
2Θ range for data collection (°)	4.616 to 49.982
Index ranges	$-10 \leq h \leq 10, -16 \leq k \leq 20, -11 \leq l \leq 11$
Reflections collected	5120
Independent reflections	1953 [R_{int} = 0.0316, R_{sigma} = 0.0718]
Data/restraints/parameters	1953/1/223
Goodness-of-fit on F²	0.929
Final R indexes [I≥2σ (I)]	R_1 = 0.0380, wR_2 = 0.0932
Final R indexes [all data]	R_1 = 0.0585, wR_2 = 0.0972
Largest diff. peak/hole (e.Å⁻³)	0.36/-0.30

Dong *et al.* reported the synthesis of a similar complex (CCDC-777866) under reflux conditions, they obtained single crystals suitable for SC-XRD only after 20 days [23]. In addition, no other experimental and theoretical studies were reported for the complex. Here, we report the synthesis of the complex in just 72 hours using the hydrothermal method [24] as an alternative time-efficient method. In addition, using the disc diffusion technique [25], antibacterial activity was examined against Gram-positive and Gram-negative bacteria strains of *Staphylococcus aureus* and *Escherichia coli,* respect-tively. Molecular docking studies were also performed against the respective protein targets to comprehend the binding activity. Computational studies were performed to find the relationship between antibacterial activity and the HOMO-LUMO energy gap. Furthermore, Hirshfeld surface analysis [26] and pharmacokinetic studies were also performed to better understand the intermolecular interactions and ADME properties [27].

2. Experimental

2.1. Materials

Copper nitrate ($Cu(NO_3)_2 \cdot 2H_2O$, 98% pure), 2,6-pyridine dicarboxylic acid (dipicolinic acid, 99%pure), benzimidazole (98% pure) and triply distilled deionized water (with specific conductance <1×10⁻⁶ S·cm⁻¹ at 25 °C) were used during synthesis. All of these compounds were of A.R. grade (purchased from S.D. Fine-Chem Limited, India) and were used without additional purification.

2.2. Instrumentations

The FT-IR spectrum was obtained at ambient temperature using a Perkin Elmer FT-IR spectrometer (RX-1) in the region 4000 to 400 cm⁻¹. The sample was pressed into a pellet after being diluted with IR grade KBr (Sigma-Aldrich, Germany). The morphology of the crystal was investigated by field emission scanning electron microscopy (FESEM, JSM-IT 100). Data for single crystal X-ray diffraction were obtained using Bruker SMART CCD area-detector diffractometer and the relevant software [28].

2.3. Synthesis of copper complex

The copper complex was synthesized hydrothermally at 120 °C in a 5 mL Teflon-lined stainless-steel autoclave under autogenous pressure. A mixture of $Cu(NO_3)_2 \cdot 2H_2O$ (241 mg, 1 mmol), dipicolinic acid (167 mg, 1 mmol), and benzimidazole (118 mg, 1 mmol) was pulverized using an agate mortar and pestle. The mixture was then poured into a 5 mL Teflon lined stainless steel autoclave and distilled water (3.0 mL) was added to it, then the mixture was stirred for about 40 min until a homogeneous suspension was obtained. The autoclave was then sealed and the reaction mixture was heated for 72 h in an automated hot air oven at 120 °C. After 72 h, the autoclave was left for approximately 10 h to cool naturally at room temperature. The initial pH of the suspension was around 3 and remained constant after the reaction was complete. The reaction mixture was filtered and washed multiple times with triply distilled deionized water and ethanol. The solid residue obtained was allowed to air dry for several hours. Yield: 379 mg (72% based on copper). Blue-colored crystals having needle-like shape, suitable for single-crystal XRD, were obtained. It was collected by hand picking under a microscope (40×). The complex obtained was completely soluble in dimethyl sulfoxide and did not melt up to 300 °C.

2.4. Single crystal structure determination

The single crystal of the complex was analyzed using a Bruker Smart Apex II X-ray single crystal diffractometer equipped with Kryoflex liquid N₂ attachment for crystal mounting. Radiation used was MoKα (λ = 0.71073 Å) and absorption multi-scan [28] was applied to all data and analysed with related softwares [28,29]. The structure of the complex was solved and refined using SHELX-97 software [28]. The crystal data of the $C_{14}H_{11}CuN_3O_5 \cdot H_2O$ complex (CCDC Depo-sition number: 2286899) was found to closely resemble the reported complex (CCDC Deposition number: 777866) [23]. The crystal data and structure refinement parameters are provided in Table 1 and the X-ray geometrical parameters (bond distance and angles) are provided in Table 2.

Table 2. Bond lengths for copper complex.

Atom	Atom	Length (Å) (Exp.)	Length (Å) (Theor.)	Atom	Atom	Length (Å) (Exp.)	Length (Å) (Theor.)
Cu1	O1	2.018(3)	2.010	C8	O3	1.224(5)	1.226
Cu1	N2	1.942(4)	1.985	C8	O2	1.266(5)	1.307
Cu1	N3	1.905(4)	1.925	N1	C7	1.314(5)	1.360
Cu1	O2	2.048(3)	2.055	N1	C5	1.367(5)	1.392
Cu1	O5	2.243(3)	2.391	C9	C10	1.363(6)	1.393
O1	C14	1.267(5)	1.305	C14	C13	1.530(6)	1.530
N2	C6	1.396(5)	1.394	C12	C11	1.369(6)	1.402
N2	C7	1.313(5)	1.320	C12	C13	1.378(6)	1.402
O4	C14	1.221(5)	1.226	C4	C5	1.400(6)	1.397
N3	C9	1.334(5)	1.333	C6	C1	1.397(6)	1.400
N3	C13	1.333(5)	1.332	C6	C5	1.386(6)	1.410
C3	C4	1.345(7)	1.393	C1	C2	1.382(7)	1.392
C3	C2	1.410(7)	1.413	C10	C11	1.381(6)	1.402
C8	C9	1.514(6)	1.529				

Table 3. Bond angles for copper complex.

Atom	Atom	Atom	Angle (°) (Exp.)	Angle (°) (Theor.)	Atom	Atom	Atom	Angle (°) (Exp.)	Angle (°) (Theor.)
O1	Cu1	O2	159.60(12)	158.02	N3	C9	C10	120.1(4)	121.23
O1	Cu1	O5	94.94(13)	94.91	C10	C9	C8	128.9(4)	129.36
N2	Cu1	O1	100.75(13)	101.23	C8	O2	Cu1	114.2(3)	114.56
N2	Cu1	O2	97.50(13)	96.58	O1	C14	C13	114.6(4)	114.92
N2	Cu1	O5	94.62(15)	94.89	O4	C14	O1	125.8(4)	124.90
N3	Cu1	O1	80.72(13)	81.00	O4	C14	C13	119.6(4)	119.63
N3	Cu1	N2	170.16(16)	170.26	C11	C12	C13	118.2(4)	119.79
N3	Cu1	O2	79.76(13)	79.11	C3	C4	C5	117.1(5)	117.94
N3	Cu1	O5	94.95(14)	93.99	N2	C6	C1	131.1(4)	130.56
O2	Cu1	O5	92.60(13)	92.79	C5	C6	N2	107.5(4)	107.90
C14	O1	Cu1	115.1(3)	116.22	C5	C6	C1	121.4(4)	120.53
C6	N2	Cu1	131.6(3)	131.63	C2	C1	C6	116.4(5)	114.33
C7	N2	Cu1	121.2(3)	120.99	C9	C10	C11	118.3(4)	116.96
C7	N2	C6	106.0(4)	105.53	C12	C11	C10	121.1(5)	120.79
C9	N3	Cu1	119.2(3)	119.67	N2	C7	N1	112.0(4)	111.57
C13	N3	Cu1	118.3(3)	119.00	N3	C13	C14	111.3(4)	110.99
C13	N3	C9	122.6(4)	122.34	N3	C13	C12	119.7(4)	117.79
C4	C3	C2	122.1(5)	122.12	C12	C13	C14	129.0(4)	130.23
O3	C8	C9	119.1(4)	119.37	C1	C2	C3	121.5(5)	119.99
O3	C8	O2	125.5(4)	126.33	N1	C5	C4	132.7(4)	133.63
O2	C8	C9	115.4(4)	114.34	N1	C5	C6	105.8(4)	107.33
C7	N1	C5	108.6(3)	107.57	C6	C5	C4	121.6(4)	123.63
N3	C9	C8	110.9(4)	111.00					

2.5. Antibacterial activities

The bacterial strains used in this investigation were *E. coli* (ATCC-25922) and *S. aureus* (ATCC-25923). Individual pure bacteria cultures were grown on nutrient agar medium at a concentration of 40 g/L. To sustain the bacterial cultures, they were subcultured on a regular basis using the same medium, then incubated at 37 °C for 24 hours before being stored at 4 °C until they were used in this experiment [30,31]. The agar well diffusion technique [30-34] was used to assess the antibacterial activity of the synthesized complex with minimal modifications [30]. Antimicrobial susceptibility was assessed using a medium made with agar (20 g/L) and Mueller Hinton (MH) broth (21 g/L) in a 1 L conical flask using the agar well diffusion technique. After preparing the medium, it was autoclaved at 120 °C for 20 minutes to sterilize it. A sterile cork borer was used to make a 6 mm hole, after which 100 μL of the solution (made by dissolving the complex in DMSO) were pipetted into triplicate wells at a concentration of 10 mg/mL. The width of the inhibition zone was measured in three different fixed directions and the mean value was obtained after incubation of the plates at 37 °C for 24-48 h.

2.6. Molecular docking

The prediction of interactions between a small molecule (ligand) and a target protein can be done computationally by using molecular docking. The interactions of a compound with a particular target of bacterial proteins, such as an enzyme or receptor crucial for bacterial growth or survival, could be usefully revealed by molecular coupling to predict antibacterial activity [35].

Auto-Dock Vina software [36] was used for molecular docking studies. The RCSB PDB (https://www.rcsb.org) was used to obtain the X-ray crystallographic structure of the receptor protein, which was then used for molecular docking studies against the synthesized complex [37]. The receptor structure was described as rigid, the grid dimensions *x*, *y* and *z* ranged from 62, 100, 88 and 54, 68, 64 with 1 Å spacing for the proteins with PDB ID-2XCS and PDB ID-1D7U, respectively [38,39]. By removing water molecules and polar hydrogen, each protein of interest was prepared [37].

2.7. Density functional theory studies

Density functional theory (DFT) is an extremely successful approach for the description of ground state properties of metals, semiconductors, and insulators [40]. Here, the structure of the complex was fully optimized using the Gaussian 16 program package [41] using the UB3LYP hybrid functional [42] at 6-31++G(d,p) [43] level of theory 6-31++G(d,p) [43] combined with the LANL2DZ [44] basis set for a heavy element like Cu. EmpiricalDispersion = GD3 [45] and TightSCF [45] criteria were applied for a better result.
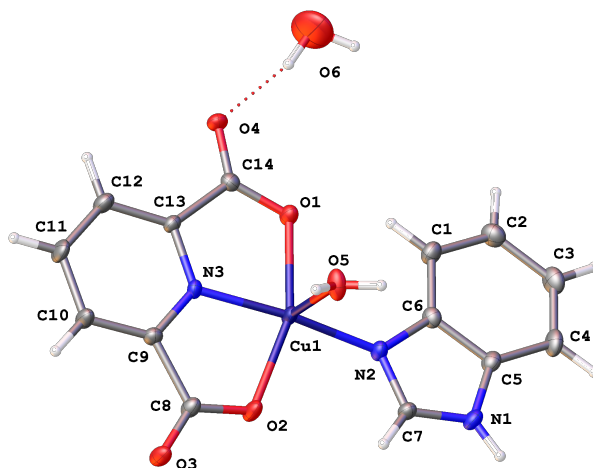
Figure 1. ORTEP representation of the asymmetric unit of the complex with the atom numbering scheme. All thermal ellipsoids are drawn at 50% probability level.

Frequency analysis was carried out using the same functional and basis set to verify the nature of optimized molecule. No imaginary frequency was found, which signifies a stationary point of minimum and the success of geometry optimization [46].

2.8. Pharmacokinetic analysis

The pharmacokinetic properties of a substance or compound, such as its absorption, distribution, metabolism, and excretion (ADME), must be evaluated prior to clinical and animal studies because they determine the potential of the substance as a drug and its activity within the body [47]. Additionally, the pharmacokinetic parameters provide important details on drug concentrations in various locations in the body over time [48]. For any chemical to be evaluated as a drug candidate, pharmacokinetic characteristics such as gastrointestinal absorption (GI), water soluble capacity (Log S), lipophilicity (Log $P_{o/w}$), CYP1A2 inhibitor, and blood-brain barrier (BBB) are crucial [49]. Therefore, the SwissADME database (http://www.sib.swiss) was used to assess the pharmacokinetic characteristics of the complex [27].

3. Results and discussion

3.1. Structural description

Single crystal X-ray diffraction studies of the complex $C_{14}H_{11}CuN_3O_5.H_2O$ revealed that it crystallizes in monoclinic form with the space group $P2_1/n$. In Figure 1, it is evident that the asymmetric unit consists of a Cu(II) ion coordinated with one *N atom* of benzimidazole, one N atom of dipicolinic acid, two O atoms of dipicolinic acid, and one O atom of water molecule. The geometry of the complex is distorted square pyramidal with a Cu(II) ion, dipicolinic acid, and benzimidazole in almost a single plane, thereby forming the base, and one water molecule is out of the plane forming the apex of the square pyramidal geometry. The dipicolinate ligands are linked to a Cu(II) ion in a tridentate *N,N,O* chelating mode, forming two 5-membered chelate rings and the benzimidazole moiety and water molecules behave as monodentate ligands, both occupying the remaining positions of a square pyramidal geometry. Both Cu-O bonds formed by the O atoms of the dipicolinic acid anion are almost of the same length (Cu1-O1 = 2.018(3) Å and Cu1-O2 = 2.048(3)Å), whereas Cu-O bond formed by the O atom of water is much higher (Cu1-O5 = 2.243(3) Å). As expected, the two Cu-N bonds (one formed by the N-atom of benzimidazole and the other formed using the N-atom of dipicolinic acid) are of different lengths (Cu1-N2 = 1.942(4) Å and Cu1-N3 = 1.905(4) Å). There is a slight distortion in the bond angles surrounding the Cu(II) ion. This may be due to the steric hindrance of the dipicolinic acid anion and the benzimidazole moiety [50]. The geometrical parameters of the obtained complex were very close to those of the reported complex [23]. The bond parameters of the reported complex are as follows; Cu1-O1 = 2.001(3), Cu1-O2 = 2.052 (3), Cu1-O5 = 2.242(3), Cu1-N2 = 1.934(3) and Cu1-N3 = 1.898(3) Å.

3.2. FT-IR spectroscopy

The broad band observed at around 3444 cm^{-1} in the FT-IR spectrum of the complex is due to the OH stretching vibrations of the coordinated water molecules [51]. The peaks observed at 3061 and 2925 cm^{-1} are due to aromatic C-H stretching vibration and C-H vibration, respectively [52]. The O-H rocking and wagging vibrations of the coordinated H$_2$O molecules in the complex were assigned a peak of around 856 cm^{-1} [53]. A broad band around 471 cm^{-1} could be attributed to Cu-O stretching vibration [51,54]. Cu-N stretching vibrations were assigned to the peak at 447 cm^{-1}, indicating that the N of imidazole and 2,6-pyridine dicarboxylic acid coordinate with the Cu(II) ion [55,56]. The characteristic bands of the carboxylate group appear at 1362 cm-1, suggesting coordination of the O atom of the 2,6 pyridine dicarboxylic acid moiety with the Cu(II) ion [51,54].

3.3. Scanning electron microscope (SEM) analysis

The FE-SEM image (Figure 2) of the complex shows the formation of large crystals of the complex, demonstrating its regular crystalline structure. The crystal grains are arranged in a unidirectional and regular pattern, as is seen in Figure 2. The crystal is arranged in a regular rod shape and has well-characterized regular faces.

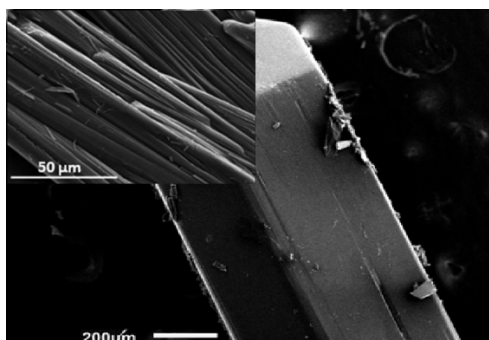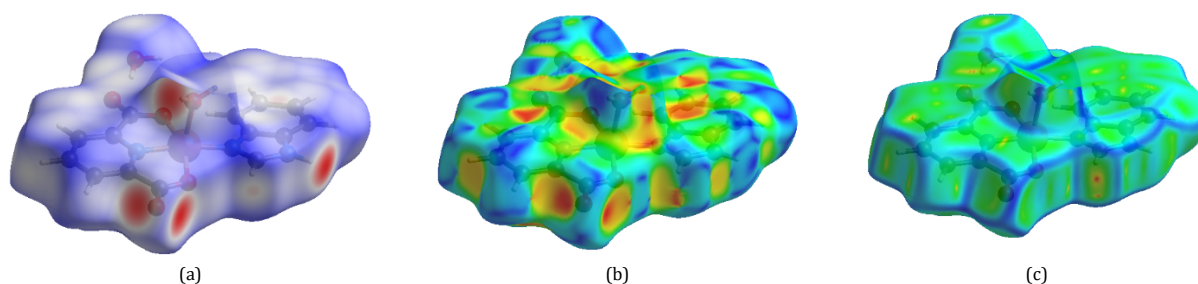#### 3.4. Hirshfeld surface analysis

The Hirshfeld surface analysis of the synthesized complex was performed and their associated two-dimensional fingerprint plots were used to predict possible intermolecular interactions. For mapping the Hirshfeld surface of a molecule, the descriptor d_{norm} was used, which includes two factors: (i) d_e, which represents the distance of any surface point nearest to

Table 4. Lipinski's properties and pharmacokinetic properties (ADME) of the title complex *.

MW	#RB	#HBD	#HBA	Violation	Log P$_{O/W}$	Log S	GI	BBB	CYP1A2	TPSA	Bioavailability score
382.82	1	3	6	0	-0.04	-3.97	High	No	Yes	94.61	0.55

* MW: Molecular weight (g/mol), #RB: Rotatable bond, #HBD: Hydrogen bond donor, #HBA: Hydrogen bond acceptor, Log PO/W: Lipophilicity (Octane/water), Log S: Solubility, GI: Gastro intestinal absorption, BBB: Blood brain barrier, CYP1A2: TPSA: Topological polar surface area.

Figure 2. FE-SEM images of the crystal. Inset: Rod-shaped crystals with well-characterized faces.

(a)   (b)   (c)

Figure 3. Molecular Hirshfeld surface: (a) d_{norm}; (b) shape index, (c) curvedness.

the internal atoms, and (ii) d_i, which represents the distance of any surface point nearest to the exterior atoms [57]. The parameter d_{norm} is calculated by the mathematical expression given below;

$$d_{norm} = (d_i – r_i^{vdw})/ r_i^{vdw} + (d_e – r_e^{vdw})/ r_e^{vdw} \qquad (1)$$

where r_i^{vdw} and r_i^{vdw} represent the van der Waals radii of atoms. On the basis of the types of intermolecular contacts, the parameter d_{norm} may have a negative or positive value. The intermolecular contacts are shorter than the van der Waals separation if the value is negative, and the contacts are larger than the van der Waals separation if the value is positive [57].

The d_{norm} shows a surface with bright red, white, and blue spots for the shortest contact, contact around the van der Waals separation, and devoid of close contacts, which appear as the primary interaction in the complex, respectively. The Hirshfeld surface is unique in crystals with spherical atomic electron densities and provides insight into the intermolecular interactions that occur in the studied molecular crystals. The surfaces have been made transparent for better visualization of the molecular moiety around which they are calculated. Figure 3 shows the molecular Hirshfeld surface for Cu(II); d_{norm}, curvedness and shape index for the Cu(II) complex, which is mapped over the d_{norm} range -0.6670 to 1.3215, curvedness range -4.0000 to 0.4000 and shape index ranges -1.0000 to 1.0000, respectively. Compared to the van der Waals sum of the two elements that share this interaction, the intense red spots in the crystal d_{norm} maps indicate the presence of significantly short intermolecular contacts. In the corresponding fingerprint plots (shown in Figure 4), the red spots appeared as sharp spikes and were found to be associated with the polar O···H hydrogen bonding interactions. The other less important intermolecular interactions appeared in the d_{norm} map as faded

red spots, and the broad peaks in the fingerprint plots are attributed to the hydrophobic C···H and H···H interactions. Figure 4 shows a graphical representation of the complete quantitative determination of all possible intermolecular contacts. It is evident that the O···H (30.6%), H···H (36.4%), and C···H (12.6%) contacts contributed the most to the intermolecular interactions, indicating that these contacts are important in the molecular packing of the reported complex [58].
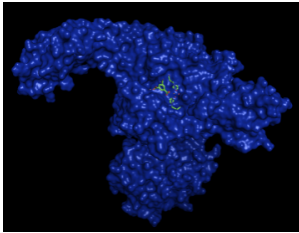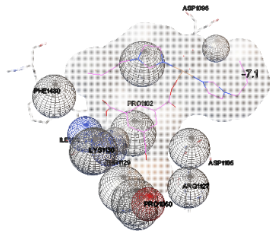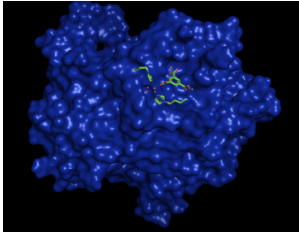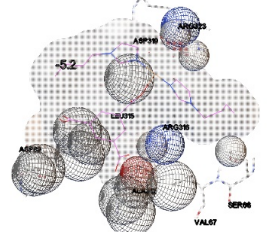
3.5. Pharmacokinetic properties

An *in silico* ADME prediction study has been performed on the copper complex. An important pharmacokinetic parameter for any compound is its bioavailability score, which was calculated using Swiss ADME software [27] and evaluated several factors such as molecular weight, hydrogen donor and acceptors, as well as rotatable bonds, lipophilicity, gastrointestinal absorption, water soluble capacity (Log S), CYP1A2 inhibitor, blood-brain barrier (BBB) [33]. It is evident from Table 4 that the complex with a bioavailability score of 55% has a consensus lipophilicity value (Log P$_{O/W}$) of -0.04. There are no apparent violations of the Lipinski rule in the title complex, indicating that this compound has the potential to be exploited as a candidate medicine [47].

3.6. Molecular docking studies

The Auto Dock Vina program was used to investigate how the copper complex interacted with different protein receptors [36]. The crystal structures of the required target proteins were retrieved from the protein data bank (PDB IDS-2XCS and 1D7U) in order to evaluate the antimicrobial activity [38,39].

Table 5. Binding affinity of the complex with different proteins.

PDB ID	Binding energy (Kcal/mol)	Amino acid residues	Molecular surface view and the molecular interactions
2XCS	-7.1	PHE1480, PRO1102, ASP1096, ASP1105, ARG1127, PRO1060, LYS1130, THR1129	
1D7U	-5.2	ASP319, ARG323, ARG316, LEU315, ASP89, VAL67, SER66	
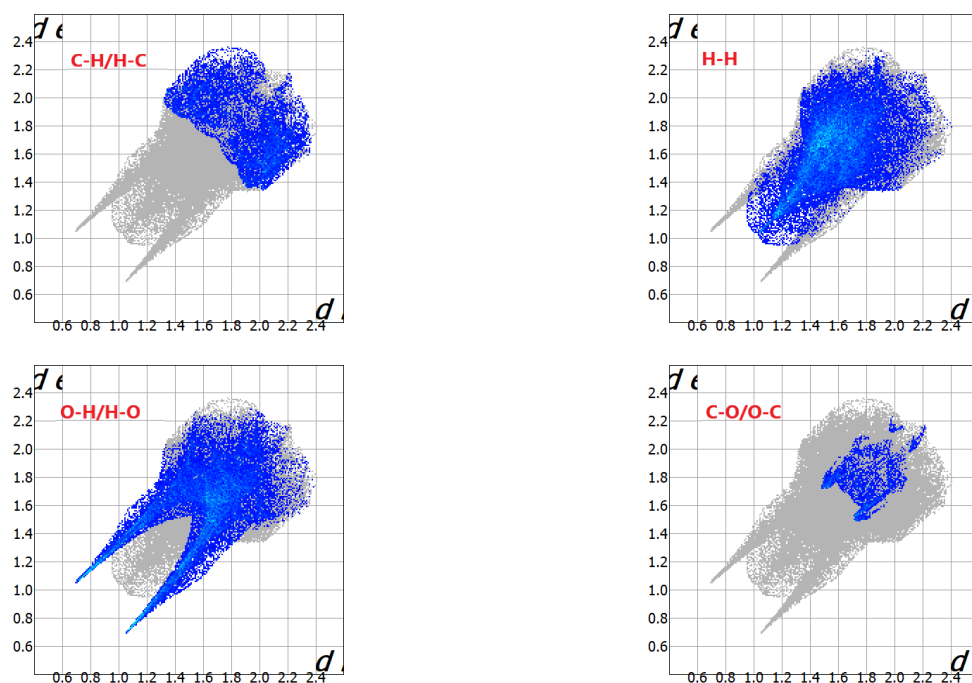
Figure 4. 2D Fingerprint plots of the complex.

Dialkylglycine decarboxylase (PDB ID: 1D7U) is one of the proteins that is frequently targeted by bacteria. Furthermore, a crystal structure of GSK299423 and the DNA-bound *S. aureus gyrase* complex were used [38,39]. The docking score for dialkylglycine decarboxylase (PDB identification 1D7U) was found to be -5.2 kcal/mol, while the docking score for the *S. aureus gyrase* complex with DNA (PDB identifier 2XCS) was determined to be -7.1 kcal/mol (Table 5). The results obtained indicate that the synthesized Cu(II) has a strong interaction with bacterial proteins.

3.7. Antibacterial activity

The disc diffusion method was used to examine the complex under study for its *in vitro* biological screening effects on a variety of bacterial species. In terms of antibacterial species, the title complex has good activity. The complex shows anti-bacterial activity against the Gram-negative bacterial isolate *E. coli* with an inhibition zone diameter of 11 mm and the Gram-positive bacterial isolate *S. aureus* with an inhibition zone diameter of 18 mm. The MIC values for the complex were checked and it was found that it shows MIC 3 mg/mL in the case of *S. aureus* and 2 mg/mL in the case of *E. coli.*

3.8. Computational studies

The optimized geometry of the Cu(II) complex is shown in Figure 5. The penta-coordinated Cu(II) complex adopts a square pyramidal structure, which is consistent with the structure obtained from a single-crystal X-ray diffraction (XRD) study.

To obtain more information about the molecular structure, excitation properties, and electron transport in the studied system, frontier molecular orbitals (HOMO and LUMO) analysis has been carried out [59,60].

Table 6. The HOMO-LUMO orbital energies, ΔE, ionisation potential (IP), electron affinity (EA), chemical potential (μ), global hardness (η), and global electrophillicity power (ω) at the UB3LYP/6-31++G(d,p) level of theory.

Parameters	Energy (eV)
E_{HOMO}	-0.24 eV
E_{LUMO}	-0.08 eV
ΔE	0.17 eV
Ionization potential (IP)	-0.24 eV
Electron affinity (EA)	0.08 eV
Chemical potential (μ)	-0.16 eV
Global hardness (ή)	0.08 eV
Electrophilicity power (ω)	0.16 eV

Table 7. Mulliken atomic charges of complex.

Atoms	Atomic charges	Atoms	Atomic charge
Cu1	-0.077022	H18	0.074810
O2	-0.534952	C19	-0.160532
H3	0.396600	H20	0.085693
H4	0.399794	C21	0.263952
O5	-0.367602	C22	0.263961
O6	-0.490847	C23	0.238960
O7	-0.488507	H24	0.150328
O8	-0.330866	C25	0.409527
N9	0.114388	C26	-0.208152
N10	-0.013600	H27	0.048559
N11	-0.277779	C28	-0.146566
H12	0.277362	H29	0.046941
C13	0.415130	C30	-0.258159
C14	0.224906	H31	0.065073
C15	-0.106678	C32	-0.095730
H16	0.085934	H33	0.103078
C17	-0.122295	C34	0.014290
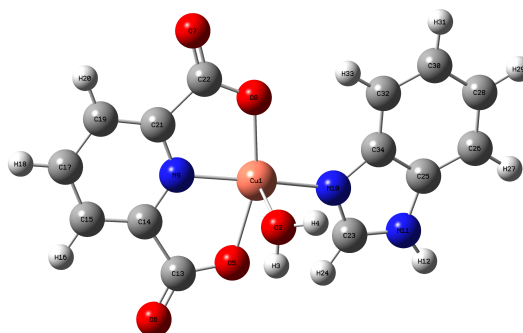
Figure 5. Optimized geometry of the copper complex.

Frontier molecular orbital theory (FMO) can also predict the optical properties and chemical stability of the complex [61]. The energy of the HOMO and LUMO orbitals of the studied system is found to be -0.24 and -0.08 eV, respectively (Table 6). The negative energy values of the HOMO and LUMO orbitals are indicators of the stability of the complex [62]. On the other hand, when the effect of optical properties is studied, a critical analysis of the energy difference in the HOMO-LUMO gap (ΔE = E_{LUMO}-E_{HOMO}) is an important parameter and for the complex studied it was found to be 0.17 eV (Figure 6). The smaller energy gap (E) between the highest occupied molecular orbital (HOMO) and the lowest unoccupied molecular orbital (LUMO) influences the molecules to absorb light in the region of higher wavelength, which is important for optoelectronic applications [63]. In addition, the HOMO-LUMO energy gap can predict the chemical hardness and softness of a molecule [64]. A low ΔE value signifies a chemically soft molecule with less stability, while a high ΔE value signifies a chemically hard molecule with high stability [65]. Polarizability increases with the increase of the softness in a molecule which facilitates to enlarge the Non linear optical (NLO) response [66].

The ionization potential (IP) and electron affinity (EA) of the organic molecule are crucial parameters that give information about the charge injection and charge transport characteristics of a molecule [61]. High EA of the conjugated molecule is used to progress the electron injection/transport and low IP of the conjugated molecule results in better hole injection/transport, which is the main parameter for the achievement of an organic light-emitting diode (OLED) [67]. The HOMO-LUMO orbital energies are directly related to the ionization potential and electron affinity of the system. To better understand, we can calculate various properties such as the chemical potential (μ), global hardness (η), and global electrophillicity power (ω) from the value of ΔE based on DFT to understand the structure and reactivity of the molecule by the following relations [62]:

$$IP = E_{HOMO} \tag{2}$$

$$EA = -E_{LUMO} \tag{3}$$

$$\mu = \frac{E_{HOMO} + E_{LUMO}}{2} \tag{4}$$

$$\eta = \frac{-E_{HOMO} + E_{LUMO}}{2} \tag{5}$$

$$\omega = \frac{\mu^2}{2\acute{\eta}} \tag{6}$$

From Table 7, it is evident that the Mulliken charges in the neighborhood of C13, C14, C21, C22, C23, C25, and C34 are more positive and thus this positive value indicates the direction of delocalization.
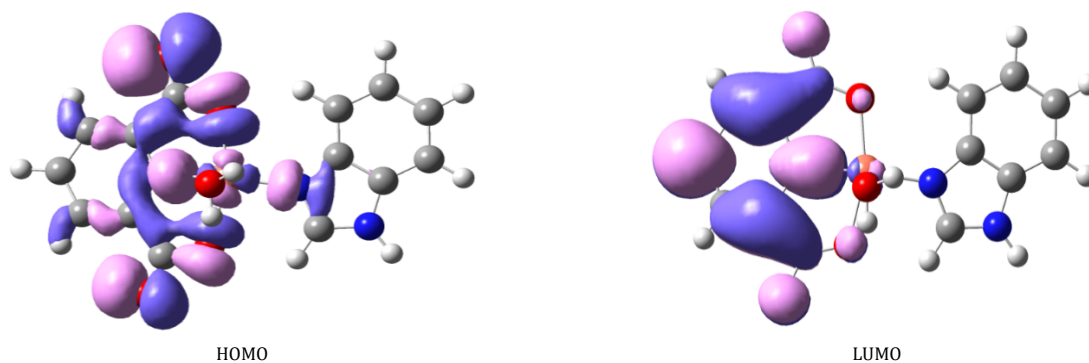
HOMO   LUMO

Figure 6. Frontier molecular orbitals of the complex studied in the gas phase at the UB3LYP/6-31++G(d,p) level of theory.
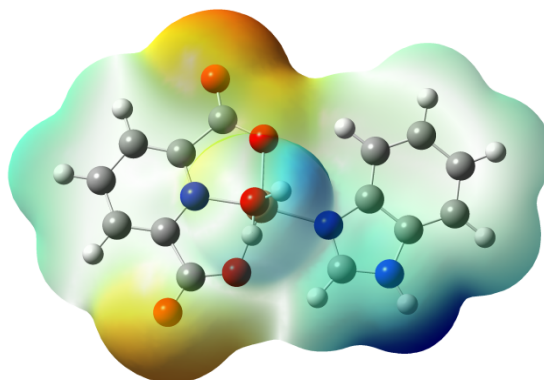

Figure 7. Molecular electrostatic potential surface diagram of the complex.

The electrostatic potential is typically visualized as a mapped surface. An electron density isosurface is colored according to the value of the electrostatic potential at each point on it [68]. Regions of large positive and negative electrostatic potential conventionally appear red and blue, respectively. While the positive (blue) portion of Molecular Electrostatic Potential (MEP) corresponds to nucleophilic reactivity, the negative (red and yellow) region is associated with electrophilic reactivity. As can be seen in Figure 7, the carboxylic group oxygen atom is the most reactive component of the molecule. The increased reactivity of this group may be due to its more electronegative character [62].

4. Conclusions

In this study, the antibacterial activities of the copper complex were explored using an extensive approach that included molecular docking, absorption, distribution, metabolism, and excretion (ADME) analysis, and density functional theory (DFT) investigations. From molecular docking studies, dialylglycine decarboxylase was discovered to have a docking score of -5.2 kcal/mol (PDB: 1D7U), whereas the *S. aureus gyrase* complex with DNA (PDB: 2XCS) had a docking score of -7.1 kcal/mol. The results show that the Cu(II) complex interacts strongly with bacterial proteins. From ADME studies, it was evident that the compound has the potential to be used as a candidate drug because there are no apparent violations of the Lipinski rule in the title complex. The HOMO-LUMO gap ($\Delta E = E_{LUMO}-E_{HOMO}$) measured using DFT calculations was found to be 0.17 eV. From antibacterial studies, the MIC values were found to be 3 mg/mL in the case of *Staphylococcus sp.* and 2 mg/mL in the case of *E. coli.* The findings of these investigations provided important information about the potential of the metal complex to be used as an antibacterial agent.

Supporting information Ⓢ

CCDC-2286899 contains the supplementary crystallographic data for this paper. These data can be obtained free of charge via www.ccdc.cam.ac.uk/data_request/cif, or by e-mailing data_request@ccdc.cam.ac.uk, or by contacting The Cambridge Crystallographic Data Centre, 12 Union Road, Cambridge CB2 1EZ, UK; fax: +44(0)1223-336033.

Disclosure statement ⒹⓈ

Conflict of interest: The authors declare that they have no conflict of interest.
Ethical approval: All ethical guidelines have been adhered.
Sample availability: Samples of the compound are available from the author.

CRediT authorship contribution statement Ⓒⓡ

Conceptualization: Anmol Chettri; Methodology: Anmol Chettri, Sudarshan Pradhan; Software: Sriparna Roy; Validation: Anmol Chettri; Formal Analysis: Anmol Chettri, Pritika Gurung; Investigation: Anmol Chettri; Resources: Anmol Chettri, Biswajit Sinha; Data Curation: Anmol Chettri; Writing - Original Draft: Anmol Chettri; Writing - Review and Editing: Anmol Chettri, Biswajit Sinha; Visualization: Anmol Chettri; Funding acquisition: Anmol Chettri, Biswajit Sinha; Supervision: Biswajit Sinha; Project Administration: Biswajit Sinha.

ORCID ⒾⒹ and Email ✉

Anmol Chettri
✉ chettrianmol5@gmail.com
ⒾⒹ https://orcid.org/0000-0002-7939-238X

Sudarshan Pradhan

✉ sudarshanpradhan43@gmail.com

🆔 https://orcid.org/0000-0002-6963-8980

Pritika Gurung

✉ pritikagurung21@gmail.com

🆔 https://orcid.org/0000-0003-2074-0711

Sriparna Roy

✉ chemsriparna26@gmail.com

🆔 https://orcid.org/0009-0001-0737-5767

Biswajit Sinha

✉ biswachem@gmail.com

🆔 https://orcid.org/0000-0003-0468-4035

References

[1]. Aakeröy, C. B.; Champness, N. R.; Janiak, C. Recent advances in crystal engineering. *CrystEngComm* **2010**, *12*, 22–43.

[2]. Wong-Foy, A. G.; Matzger, A. J.; Yaghi, O. M. Exceptional H2 saturation uptake in microporous Metal–Organic frameworks. *J. Am. Chem. Soc.* **2006**, *128*, 3494–3495.

[3]. Abrahams, B. F.; FitzGerald, N. J.; Robson, R. Cages with tetrahedron-like topology formed from the combination of cyclotricatechylene ligands with metal cations. *Angew. Chem. Int. Ed Engl.* **2010**, *49*, 2896–2899.

[4]. Deng, H.; Doonan, C. J.; Furukawa, H.; Ferreira, R. B.; Towne, J.; Knobler, C. B.; Wang, B.; Yaghi, O. M. Multiple functional groups of varying ratios in metal-organic frameworks. *Science* **2010**, *327*, 846–850.

[5]. Gándara, F.; Medina, M. E.; Snejko, N.; Gutiérrez-Puebla, E.; Proserpio, D. M.; Angeles Monge, M. Ligand dependent topology changes in six zinc coordination polymers. *CrystEngComm* **2010**, *12*, 711–719.

[6]. Niu, M.; Huang, F.; Cui, L.; Huang, P.; Yu, Y.; Wang, Y. Hydrothermal synthesis, structural characteristics, and enhanced photocatalysis of SnO2/α-Fe2O3 semiconductor nanoheterostructures. *ACS Nano* **2010**, *4*, 681–688.

[7]. Baibarac, M.; Baltog, I.; Smaranda, I.; Scocioreanu, M.; Lefrant, S. Hybrid organic–inorganic materials based on poly(o-phenylenediamine) and polyoxometallate functionalized carbon nanotubes. *J. Mol. Struct.* **2011**, *985*, 211–218.

[8]. Ngo, H. T.; Liu, X.; Jolliffe, K. A. Anion recognition and sensing with Zn(ii)–dipicolylamine complexes. *Chem. Soc. Rev.* **2012**, *41*, 4928.

[9]. Zeng, Z.; Matuschek, D.; Studer, A.; Schwickert, C.; Pöttgen, R.; Eckert, H. Synthesis and characterization of inorganic–organic hybrid materials based on the intercalation of stable organic radicals into a fluoromica clay. *Dalton Trans.* **2013**, *42*, 8585–8596.

[10]. Xu, H.; Chen, R.; Sun, Q.; Lai, W.; Su, Q.; Huang, W.; Liu, X. Recent progress in metal–organic complexes for optoelectronic applications. *Chem. Soc. Rev.* **2014**, *43*, 3259–3302.

[11]. Manikandamathavan, V. M.; Weyhermüller, T.; Parameswari, R. P.; Sathishkumar, M.; Subramanian, V.; Nair, B. U. DNA/protein interaction and cytotoxic activity of imidazole terpyridine derived Cu(ii)/Zn(ii) metal complexes. *Dalton Trans.* **2014**, *43*, 13018–13031.

[12]. Lemoine, P.; Viossat, B.; Morgant, G.; Greenaway, F. T.; Tomas, A.; Dung, N.-H.; Sorenson, J. R. J. Synthesis, crystal structure, EPR properties, and anti-convulsant activities of binuclear and mononuclear 1,10-phenanthroline and salicylate ternary copper(II) complexes. *J. Inorg. Biochem.* **2002**, *89*, 18–28.

[13]. Lavie-Cambot, A.; Cantuel, M.; Leydet, Y.; Jonusauskas, G.; Bassani, D. M.; McClenaghan, N. D. Improving the photophysical properties of copper(I) bis(phenanthroline) complexes. *Coord. Chem. Rev.* **2008**, *252*, 2572–2584.

[14]. Devereux, M.; O Shea, D.; Kellett, A.; McCann, M.; Walsh, M.; Egan, D.; Deegan, C.; Kędziora, K.; Rosair, G.; Müller-Bunz, H. Synthesis, X-ray crystal structures and biomimetic and anticancer activities of novel copper(II)benzoate complexes incorporating 2-(4′-thiazolyl)benzimidazole (thiabendazole), 2-(2-pyridyl)benzimidazole and 1,10-phenanthroline as chelating nitrogen donor ligands. *J. Inorg. Biochem.* **2007**, *101*, 881–892.

[15]. Ma, C.; Chen, C.; Liu, Q.; Liao, D.; Li, L. The first structurally characterized trinuclear dipicolinato manganese complex and its conversion into a mononuclear species by ligand substitution. *Eur. J. Inorg. Chem.* **2003**, *2003*, 1227–1231.

[16]. Ranjbar, M.; Aghabozorg, H.; Moghimi, A. A seven-coordinate pyridine-2,6-dicarboxylate-bridged cadmium(II) complex, at 110 K. *Acta Crystallogr. Sect. E Struct. Rep. Online* **2002**, *58*, m304–m306.

[17]. Ma, C.; Fan, C.; Chen, C.; Liu, Q. Aqua(dipicolinato-κ3O2,N,O6)(1,10-phenanthroline-κ2N,N′)manganese(II) monohydrate. *Acta Crystallogr. C* **2002**, *58*, m553–m555.

[18]. Koman, M.; Melník, M.; Moncol, J. Crystal and molecular structure of copper(II)(pyridine-2,6-dicarboxylato)(2,6-dimethanolpyridine). *Inorg. Chem. Commun.* **2000**, *3*, 262–266.

[19]. Kanai, Y. Simultaneous determination of iron(II) and iron(III) oxides in geological materials by ion chromatography. *Analyst* **1990**, *115*, 809–812.

[20]. Hindle, A. A.; Hall, E. A. H. Dipicolinic acid (DPA) assay revisited and appraised for spore detection. *Analyst* **1999**, *124*, 1599–1604.

[21]. Anandan, K.; Vittal, R. R. Endophytic Paenibacillus amylolyticus KMCLE06 extracted dipicolinic acid as antibacterial agent derived via dipicolinic acid synthetase gene. *Curr. Microbiol.* **2019**, *76*, 178–186.

[22]. Şahin, E.; İde, S.; Kurt, M.; Yurdakul, Ş. Structural investigation of dibromobis(benzimidazole)Zn(II) complex. *J. Mol. Struct.* **2002**, *616*, 259–264.

[23]. Dong, G.-Y.; Fan, L.-H.; Yang, L.-X.; Khan, I. U. Aqua(1H-benzimidazole-κN3)(pyridine-2,6-dicarboxylato-κ3O2,N,O6)copper(II) 0.75-hydrate. *Acta Crystallogr. Sect. E Struct. Rep. Online* **2010**, *66*, m532–m532.

[24]. Feng, S.; Xu, R. New materials in hydrothermal synthesis. *Acc. Chem. Res.* **2001**, *34*, 239–247.

[25]. Klančnik, A.; Piskernik, S.; Jeršek, B.; Možina, S. S. Evaluation of diffusion and dilution methods to determine the antibacterial activity of plant extracts. *J. Microbiol. Methods* **2010**, *81*, 121–126.

[26]. Spackman, M. A.; Jayatilaka, D. Hirshfeld surface analysis. *CrystEngComm* **2009**, *11*, 19–32.

[27]. Paul Gleeson, M.; Hersey, A.; Hannongbua, S. In-silico ADME models: A general assessment of their utility in drug discovery applications. *Curr. Top. Med. Chem.* **2011**, *11*, 358–381.

[28]. Sheldrick, G. M. (1997). SHELX-97. University of Göttingen, Germany.

[29]. Altomare, A.; Burla, M. C.; Camalli, M.; Cascarano, G. L.; Giacovazzo, C.; Guagliardi, A.; Moliterni, A. G. G.; Polidori, G.; Spagna, R. SIR97: a new tool for crystal structure determination and refinement. *J. Appl. Crystallogr.* **1999**, *32*, 115–119.

[30]. Lala, M.; Modak, D.; Paul, S.; Sarkar, I.; Dutta, A.; Kumar, A.; Bhattacharjee, S.; Sen, A. Potent bioactive methanolic extract of wild orange (Citrus macroptera Mont.) shows antioxidative, anti-inflammatory, and antimicrobial properties in in vitro, in vivo, and in silico studies. *Bull. Natl. Res. Cent.* **2020**, *44*, 81.

[31]. Boyanova, L.; Gergova, G.; Nikolov, R.; Derejian, S.; Lazarova, E.; Katsarov, N.; Mitov, I.; Krastev, Z. Activity of Bulgarian propolis against 94 Helicobacter pylori strains in vitro by agar-well diffusion, agar dilution and disc diffusion methods. *J. Med. Microbiol.* **2005**, *54*, 481–483.

[32]. Mini Shobi, T.; Gowdu Viswanathan, M. B. Antibacterial activity of di-butyl phthalate isolated from Begonia malabarica. *J. Appl. Biotechnol. Bioeng.* **2018**, *5 (2)*, 101–104.

[33]. Jiang, Q. Natural forms of vitamin E: metabolism, antioxidant, and anti-inflammatory activities and their role in disease prevention and therapy. *Free Radic. Biol. Med.* **2014**, *72*, 76–90.

[34]. Panda, S.; Jafri, M.; Kar, A.; Meheta, B. K. Thyroid inhibitory, antiperoxidative and hypoglycemic effects of stigmasterol isolated from Butea monosperma. *Fitoterapia* **2009**, *80*, 123–126.

[35]. Pisano; Kumar; Medda; Gatto; Pal; Fais; Era; Cosentino; Uriarte; Santana; Pintus; Matos Antibacterial activity and molecular docking studies of a selected series of hydroxy-3-arylcoumarins. *Molecules* **2019**, *24*, 2815.

[36]. Trott, O.; Olson, A. J. AutoDock Vina: Improving the speed and accuracy of docking with a new scoring function, efficient optimization, and multithreading. *J. Comput. Chem.* **2009**, *31*, 455–461.

[37]. Kouranov, A. The RCSB PDB information portal for structural genomics. *Nucleic Acids Res.* **2006**, *34*, D302–D305.

[38]. Bax, B. D.; Chan, P. F.; Eggleston, D. S.; Fosberry, A.; Gentry, D. R.; Gorrec, F.; Giordano, I.; Hann, M. M.; Hennessy, A.; Hibbs, M.; Huang, J.; Jones, E.; Jones, J.; Brown, K. K.; Lewis, C. J.; May, E. W.; Singh, O.; Spitzfaden, C.; Shen, C.; Shillings, A.; Theobald, A. F.; Wohlkonig, A.; Pearson, N. D.; Gwynn, M. N. The 2.1A crystal structure of S. aureus Gyrase complex with GSK299423 and DNA **2010**. https://doi.org/10.2210/pdb2xcs/pdb (accessed April 9, 2023).

[39]. Malashkevich, V. N.; Strop, P.; Keller, J. W.; Jansonius, J. N.; Toney, M. D. Crystal structures of dialkylglycine decarboxylase inhibitor complexes 1 1Edited by R. Huber. *J. Mol. Biol.* **1999**, *294*, 193–200.

[40]. Marini, A.; Hogan, C.; Grüning, M.; Varsano, D. yambo: An ab initio tool for excited state calculations. *Comput. Phys. Commun.* **2009**, *180*, 1392–1403.

[41]. Frisch, M. J.; Trucks, G. W.; Schlegel, H. B.; Scuseria, G. E.; Robb, M. A.; Cheeseman, J. R.; Montgomery, J. A.; Vreven, T.; Kudin, K. N.; Burant, J. C.; Millam, J. M.; Iyengar, S. S.; Tomasi, J.; Barone, V.; Mennucci, B.; Cossi, M.; Scalmani, G.; Rega, N.; Petersson, G. A.; Nakatsuji, H.; Hada, M.; Ehara, M.; Toyota, K.; Fukuda, R.; Hasegawa, J.; Ishida, M.; Nakajima, T.; Honda, Y.; Kitao, O.; Nakai, H.; Klene, M.; Li, X.; Knox, J. E.; Hratchian, H. P.; Cross, J. B.; Adamo, C.; Jaramillo, J.; Gomperts, R.; Stratmann, R. E.; Yazyev, O.; Austin, A. J.; Cammi, R.; Pomelli, C.; Ochterski, J. W.; Ayala, P. Y.; Morokuma, K.; Voth, G. A.; Salvador, P.; Dannenberg, J. J.; Zakrzewski, V. G.; Dapprich, S.; Daniels, A. D.; Strain, M. C.; Farkas, O.; Malick, D. K.; Rabuck, A. D.; Raghavachari, K.; Foresman, J. B.; Ortiz, J. V.; Cui, Q.; Baboul, A. G.; Clifford, S.; Cioslowski, J.; Stefanov, B. B.; Liu, G.; Liashenko, A.; Piskorz, P.; Komaromi, I.; Martin, R. L.; Fox, D. J.; Keith, T.; Al-Laham, M. A.; Peng, C. Y.; Nanayakkara, A.; Challacombe, M.; Gill, P. M. W.; Johnson, B.; Chen, W.;

Wong, M. W.; Gonzalez, C.; Pople, J. A. Gaussian 16, Inc., Wallingford CT, 2016.

[42]. Ullah, H.; Shah, A.-U.-H. A.; Bilal, S.; Ayub, K. Doping and dedoping processes of polypyrrole: DFT study with hybrid functionals. *J. Phys. Chem. C Nanomater. Interfaces* **2014**, *118*, 17819–17830.

[43]. Frisch, M. J.; Pople, J. A.; Binkley, J. S. Self-consistent molecular orbital methods 25. Supplementary functions for Gaussian basis sets. *J. Chem. Phys.* **1984**, *80*, 3265–3269.

[44]. Chiodo, S.; Russo, N.; Sicilia, E. LANL2DZ basis sets recontracted in the framework of density functional theory. *J. Chem. Phys.* **2006**, *125*, 104107.

[45]. Aydin, M.; Akins, D. L. DFT studies on solvent dependence of electronic absorption spectra of free-base and protonated porphyrin. *Comput. Theor. Chem.* **2018**, *1132*, 12–22.

[46]. Hari, S. In silico molecular docking and ADME/T analysis of plant compounds against IL17A and IL18 targets in gouty arthritis. *J. Appl. Pharm. Sci.* **2019**, *9*, 18–26.

[47]. Abdulrahman, H. L.; Uzairu, A.; Uba, S. Computational pharmacokinetic analysis on some newly designed 2-anilinopyrimidine derivative compounds as anti-triple-negative breast cancer drug compounds. *Bull. Natl. Res. Cent.* **2020**, *44*, 63.

[48]. Boussery, K.; Belpaire, F. M.; Van de Voorde, J. Physiological aspects determining the pharmacokinetic properties of drugs. In *The Practice of Medicinal Chemistry*; Elsevier, 2008; pp. 635–654.

[49]. Ntie-Kang, F.; Lifongo, L. L.; Mbah, J. A.; Owono Owono, L. C.; Megnassan, E.; Mbaze, L. M.; Judson, P. N.; Sippl, W.; Efange, S. M. N. In silico drug metabolism and pharmacokinetic profiles of natural products from medicinal plants in the Congo basin. *In Silico Pharmacol.* **2013**, *1*, 1.

[50]. Kamath, A.; Brahman, D.; Pilet, G.; Sinha, B.; Tamang, A. [Bis(picolinate-κN:O)Copper(II)] di(benzene1,3,5- tricarboxylic acid): Hydrothermal synthesis, structural characterization, magnetic properties and DFT study. *J. Mol. Struct.* **2018**, *1165*, 228–235.

[51]. Silverstein, R. M.; Webster, F. X.; Kiemle, D. J.; Bryce, D. L. *Spectrometric identification of organic compounds*; 8th ed.; John Wiley & Sons: Chichester, England, 2014.

[52]. Kamath, A.; Pilet, G.; Tamang, A.; Sinha, B. [Diaquo(3,5-dinitrobenzoato-κ1O1)(1,10-phenanthroline-κ2N1:N10)copper(II)] 3,5-dinitrobenzoate: Hydrothermal synthesis, crystal structure and magnetic properties. *J. Mol. Struct.* **2020**, *1199*, 126933.

[53]. Frost, R. L.; Locos, O. B.; Ruan, H.; Kloprogge, J. T. Near-infrared and mid-infrared spectroscopic study of sepiolites and palygorskites. *Vib. Spectrosc.* **2001**, *27*, 1–13.

[54]. Adams, D. M. *Metal-Ligand and Related Vibrations: A Critical Survey of the Infrared and Raman Spectra of Metallic and Organometallic Compounds*; St Martin's Press: New York, NY, 1968.

[55]. Bellamy, L. *The infra-red spectra of complex molecules*; 1975th ed.; Springer: Dordrecht, Netherlands, 1975.

[56]. Nakamoto, K.; Fujita, J.; Tanaka, S.; Kobayashi, M. Infrared spectra of metallic complexes. IV. Comparison of the infrared spectra of unidentate and bidentate metallic complexes. *J. Am. Chem. Soc.* **1957**, *79*, 4904–4908.

[57]. McKinnon, J. J.; Jayatilaka, D.; Spackman, M. A. Towards quantitative analysis of intermolecular interactions with Hirshfeld surfaces. *Chem. Commun. (Camb.)* **2007**, 3814–3816.

[58]. Kamath, A.; Brahman, D.; Chhetri, S.; McArdle, P.; Sinha, B. [Diaquobis(p-hydroxybenzoato-κ1O1)(1-methylimidazole-κ1N1)copper(II)]: Synthesis, crystal structure, catalytic activity and DFT study. *J. Mol. Struct.* **2022**, *1247*, 131323.

[59]. SenthilKannan, K.; Sivaramakrishnan, V.; Kalaipoonguzhali, V.; Chinnadurai, M.; Kannan, S. Electronic transport, HOMO–LUMO and computational studies of CuS monowire for nano device fabrication by DFT approach. *Mater. Today* **2020**, *33*, 2746–2749.

[60]. Gould, T.; Hashimi, Z.; Kronik, L.; Dale, S. G. Single excitation energies obtained from the ensemble "HOMO–LUMO gap": Exact results and approximations. *J. Phys. Chem. Lett.* **2022**, *13*, 2452–2458.

[61]. Sutradhar, T.; Misra, A. Role of electron-donating and electron-withdrawing groups in tuning the optoelectronic properties of difluoroboron–napthyridine analogues. *J. Phys. Chem. A* **2018**, *122*, 4111–4120.

[62]. Suresh, C. H.; Remya, G. S.; Anjalikrishna, P. K. Molecular electrostatic potential analysis: A powerful tool to interpret and predict chemical reactivity. Wiley Interdiscip. *Rev. Comput. Mol. Sci.* **2022**, *12*, e1601.

[63]. Sun, W.; Ma, Z.; Dang, D.; Zhu, W.; Andersson, M. R.; Zhang, F.; Wang, E. An alternating D–A1–D–A2 copolymer containing two electron-deficient moieties for efficient polymer solar cells. *J. Mater. Chem. A Mater. Energy Sustain.* **2013**, *1*, 11141–11144.

[64]. Chattaraj, P. K.; Roy, D. R. Update 1 of: Electrophilicity index. *Chem. Rev.* **2007**, *107*, PR46–PR74.

[65]. Yourdkhani, S.; Korona, T.; Hadipour, N. L. Structure and energetics of complexes of B12N12 with hydrogen halides—SAPT(DFT) and MP2 study. *J. Phys. Chem. A* **2015**, *119*, 6446–6467.

[66]. He, Q.; Li, Q.; Khene, S.; Ren, X.; López-Suárez, F. E.; Lozano-Castelló, D.; Bueno-López, A.; Wu, G. High-loading cobalt oxide coupled with nitrogen-doped graphene for oxygen reduction in anion-exchange-membrane alkaline fuel cells. *J. Phys. Chem. C Nanomater. Interfaces* **2013**, *117*, 8697–8707.

[67]. Würthner, F.; Schmidt, R. Electronic and crystal engineering of acenes for solution-processible self-assembling organic semiconductors. *Chemphyschem* **2006**, *7*, 793–797.

[68]. Kenouche, S.; Sandoval-Yañez, C.; Martínez-Araya, J. I. The antioxidant capacity of myricetin. A molecular electrostatic potential analysis based on DFT calculations. *Chem. Phys. Lett.* **2022**, *801*, 139708.